

Supplemental materials for seismic evidence for craton chiseling and displacement of lithospheric mantle by the Tintina Fault in the Northern Canadian Cordillera

Clément Estève¹, Pascal Audet¹, Andrew J. Schaeffer², Derek L. Schutt³, Richard C. Aster³ and Joel F. Cubley⁴

¹*Department of Earth and Environmental Sciences, University of Ottawa, Ottawa, Ontario, Canada*

²*Geological Survey of Canada, Pacific Division, Natural Resources Canada, Sidney, British Columbia, Canada*

³*Department of Geosciences, Colorado State University, Fort Collins, Colorado, USA*

⁴*Centre for Northern Innovation in Mining, Yukon College, Whitehorse, Yukon, Canada*

TELESEISMIC SHEAR WAVE SPLITTING ANALYSIS

Shear waves travelling through Earth have the property to split into two perpendicularly polarized waves because anisotropic media are birefringent. One shear wave will travel along the fast axis direction of propagation (Φ) whereas the other perpendicular shear wave will travel along the slow axis direction of propagation. As the two shear waves propagate through an anisotropic medium, a delay time will accumulate (δt). At the Earth's surface, it is therefore possible to measure the two splitting parameters (δt and Φ). The magnitude of the delay time depends on the thickness of the anisotropic medium and the fast axis direction is related to the orientation of the anisotropic medium. Shear wave splitting measurements provide information on the upper mantle deformation. However, this technique has limitations. For teleseismic shear

23 waves, the calculated splitting estimates is an integrated value along the ray path on the receiver
24 side from the Core-Mantle Boundary (CMB) up to the surface. Therefore, teleseismic shear
25 waves record both lithospheric and asthenospheric deformations.

26 In this study, we calculated splitting estimates for 45 stations located across northwestern
27 Canada (Table DR1). We used teleseismic earthquakes of magnitude $M \geq 6.0$ in the angular
28 epicentral distance $85^\circ \leq \Delta \leq 120^\circ$ that occurred between January 2014 and August 2019. We
29 only selected waveforms with a Signal-to-Noise Ratio (SNR) greater than 7.5 dB. Waveforms
30 were then rotated into the three-dimensional ray system (LQT). We calculated SKS splitting
31 parameters for each station using SplitPy (Audet and Schaeffer, 2019), a Python version of
32 SplitLab (Wüstefeld et al., 2008). SplitPy removes the effect of seismic anisotropy using two
33 different techniques: the rotation-correlation technique (RC; Bowman and Ando, 1987) and the
34 minimum energy technique (SC; Silver and Chan, 1991). The two techniques calculate a grid-
35 search for the splitting parameters (δt and Φ), which best removes the effect of splitting. The
36 rotation-correlation technique uses the maximization of the cross-correlation coefficient between
37 the waveforms on the radial Q and transverse T components. The minimum energy technique
38 searches for the minimum energy of displacement on the transverse component.

39 In order to determine if the resulting splits are either null or non-null measurements,
40 SplitPy compares the delay times ($\rho = \delta t_{RC} / \delta t_{SC}$) and the azimuth of fast axis estimates ($\delta\Phi =$
41 $\Phi_{SC} - \Phi_{RC}$) from both techniques. A teleseismic null measurement requires that (1) the SNR of
42 the tangential component of the waveform is < 3 dB or (2) $\delta\Phi \approx 45^\circ$ and ρ is small. A teleseismic
43 non-null measurement requires that (1) the $\rho > 0.7$ and (2) $\delta\Phi < 22.5^\circ$. Null and non-null
44 measurements are then qualitatively evaluated as “Good”, “Fair” and “Poor”. For non-null
45 measurements, we have $0.8 < \rho < 1.1$ and $\delta\Phi < 8^\circ$ for “good” measurements; $0.7 < \rho < 1.2$ and

$\delta\Phi < 15^\circ$ for “fair” measurements; and “poor” otherwise. For nulls, we have $0 < \rho < 0.2$ and $37^\circ < \delta\Phi < 53^\circ$ for “good” nulls; $0 < \rho < 0.3$ and $32^\circ < \delta\Phi < 58^\circ$ for “fair” nulls; and “poor” otherwise.

Figure DR1 shows an example of a “good” measurement for an earthquake that occurred 24 September 2016 ($M_w = 6.9$). The center panels show results for the rotation-correlation technique (RC). The lower panels show results for the minimum energy technique (SC). We separately calculated a vector average of all “fair” and “good” non-null measurements for both techniques, and obtain final estimates by vector averaging the results of both techniques into a single estimate of δt and Φ for each station. Figures DR2A and DR2B show all the resulting “fair” and “good” non-null measurements for the RC and the SC techniques, respectively.

Null measurements provide additional information on the upper mantle structure beneath the seismic station. A null measurement occurs if the shear wave propagates in an isotropic medium and/or the shear wave polarization is aligned with the fast or slow axis direction in the anisotropic medium (Wüstefeld and Bokermann, 2007). Figure DR3 shows the back-azimuth of all “good” null measurements (black bars) along with the vector-averaged estimates (red bars). The back-azimuth distribution of all “good” null measurements are either aligned or perpendicular to the fast axis direction, which gives us confidence in our results. Figure DR4 shows all multievent average results of teleseismic shear-wave splitting from this study and from the compilation of shear-wave splitting estimates (Audet et al., 2016; Courtier et al., 2010; Rasendra et al., 2014; Snyder and Bruneton, 2007 and Venereau et al., 2019). Figure DR5 shows the stations for which the splitting parameters are projected along cross sections A-A’, B-B’ and C-C’ (Figure 3).

TELESEISMIC P-WAVE TOMOGRAPHY

In this study, we use the teleseismic P-wave tomography model of Estève et al., (2020). The P-wave data set consists of 127,138 delay times from 2,627 earthquakes with magnitude $M_w \geq 5.5$ spanning the angular epicentral distance range $30^\circ \leq \Delta \leq 90^\circ$ that occurred between 2000 and 2018. The three-dimensional isotropic velocity structure underlying northwestern Canada is calculated using VanDecar's inversion procedure (VanDecar, 1991). The relative delay times are inverted simultaneously for slowness perturbations, station static terms and source terms.

The P-wave model is parameterized with splines under tension constrained at a series of regular nodes. The grid extends from 51°N to 77°N in latitude, from -156°W to -94°W in longitude and from the surface to 1300 km depth. The grid has 27, 76 and 103 knots in the radius, latitude and longitude direction resulting in 211,356 knots. The inner region of the grid is sampled every 0.25° of latitude, 0.5° of longitude and every 33 km.

This inverse problem is strongly under-determined and is solved through regularization. Here, three types of regularization are applied: smoothing, flattening and damping. In order to find the preferred model, a trade-off area is generated from 72 inversions (see Estève et al., 2020 for more details). We use 2000 conjugate gradient iterations and 10 down-weighting iterations in order to get a stable solution. The final P-wave model explains 97.33 % of the RMS of the relative arrival time residuals.

Resolution of such tomographic inversion problem depends strongly on the ray geometry, and the back-azimuth distribution of teleseismic earthquakes. For a qualitative assessment of resolution, synthetic checkerboard and structural tests are performed. We generate a synthetic model consisting of an alternating checkerboard pattern with slow and fast P-wave anomalies that are $\pm 5\%$ at 200, 400 and 600 km depth (Fig. DR6A). These synthetic anomalies have a

radius of 50 km are defined by a Gaussian function across their diameter. Gaussian noise with a standard deviation of 0.03s was also added to the P-wave data set in order to mimic the noise that occurs in the real travel-time measurements.

The recovery of the synthetic anomalies is excellent across the Tintina and Denali faults and in the southwestern region of the P-wave model (Fig. DR6B). East of the Cordillera Deformation Front (CDF), stripes of anomalies oriented northeast-southwest show the effect of a poor station coverage and reflect the back-azimuth distribution in the teleseismic data.

Figure DR7 shows the input and output of the P-wave structural test. This structural test is performed to assess the robustness of longer-wavelength features and the effect of smearing (inherent to the technique) in the real model. The output synthetic model shows excellent lateral resolution between the surface and 200 km depth and at greater depths between 450 km and 650 km depth.

CALCULATION OF THERMAL LENGTH SCALE

To estimate the characteristic thermal diffusion length, we use the formula $l = \sqrt{\kappa\tau}$, where l is the diffusion length, κ is the thermal diffusivity of peridotite, and τ is the time over which the diffusion occurs, assumed to be 37 M.yrs. Peridotite is highly (~20%) anisotropic in thermal diffusivity. If we assume the measured shear wave splitting fast axis corresponds to the most thermally diffusive axis (Gilbert et al., 2003), then diffusivity should be minimized along the direction perpendicular to the Tintina Fault. For a 1000°C temperature (diffusivity decreases with increasing temperature), at a 1 GPa pressure (diffusivity increases slightly with pressure) a reasonable diffusivity for spinel lherzolite is $5 \times 10^{-7} \text{ m}^2 \text{ s}^{-1}$. This leads to a conservative estimate for characteristic length of 22 km. If the maximum thermal diffusivity axis is not aligned parallel

to the Tintina Fault, or if diffusivity anisotropy is minimal, then diffusivity and the characteristic length will be larger (Gibert, 2003).

COMPARISON OF NCC WITH CRATONIC XENOLITHS

To investigate the feasibility of seismically observable compositional variations in the lithosphere, we consider two sets of xenoliths. The first is a collection of 345 xenoliths associated with the Canadian Cordillera (Francis et al., 2010) which we take to approximate the composition of the lower velocity non-cratonic mantle in the region. For a representation of the composition of cratonic mantle, we use 45 harzburgite xenoliths from Wiedemann Fjord, Greenland (Canil, 2004). These xenoliths have been noted to have similar olivine Mg# to the Parry Peninsula xenoliths from the Mackenzie Craton (Liu et al., 2018).

We use *Perple_X* (Connolly, 1990) to calculate the P-wave velocity for each sample using the *stx11ver.dat* database (Stixrude and Lithgow-Bertelloni, 2010), at 10000 kbar and 800°C, roughly at the conditions of the uppermost mantle lithosphere. We chose to use the *stx11ver.dat* database because it is widely used in the seismological literature (e.g. Ma et al., 2020) and does a fairly good job of estimating velocity for a given composition. However, it approximates the composition of the mantle as only six oxides: SiO₂, MgO, FeO, CaO, Al₂O₃, and Na₂O. An alternative approach is to use the *hp62.dat* database (Holland and Powell, 2011). This considers a much fuller range of composition but is not widely used in seismology because it produces less accurate mantle velocity estimates.

While neither database is ideal, our tests show in both cases there is about a 2% increase in velocity between the Cordilleran and cratonic xenoliths (Figure DR8). This suggests the hypothesis that the Tintina fault bounds compositional variations is feasible.

138

139 **REFERENCES**

- 140 Audet, P., Sole, C., and Schaeffer, A.J, 2016, Control of lithospheric inheritance on neotectonic
141 activity in northwestern Canada?: *Geology*, v. 44, p. 807–810,
142 <https://doi.org/10.1130/G38118.1>.
- 143 Audet P., and Schaeffer A.J., 2019, SplitPy: Software for teleseismic shear-wave splitting
144 analysis, <https://doi.org/10.5281/zenodo.3564780>.
- 145 Bowman, J.R., Ando, M., 1987, Shear-wave splitting in the upper-mantle wedge above the
146 Tonga subduction zone, *Geophysical Journal International*, v. 88, p. 25–41,
147 <https://doi.org/10.1111/j.1365-246X.1987.tb01367.x>.
- 148 Canil, D., 2004, Mildly incompatible elements in peridotites and the origins of mantle
149 lithosphere: *Lithos*, v. 77, p. 375-393, <https://doi.org/10.1016/j.lithos.2004.04.014>.
- 150 Connolly, J.A.D., 1990, Multivariable phase diagrams; an algorithm based on generalized
151 thermodynamics: *American Journal of Science*, v. 290, p. 666-718,
152 <https://doi.org/10.2475/ajs.290.6.666>.
- 153 Courtier, A.M., Gaherty, J.B., Revenaugh, J., Bostock, M.G., and Garnero, E.J., 2010, Seismic
154 anisotropy associated with continental lithosphere accretion beneath the CANOE array,
155 northwestern Canada: *Geology*, v. 38, p. 887–890, <https://doi.org/10.1130/G31120.1>.
- 156 Estève, C., Audet, P., Schaeffer, A.J, Schutt, D., Aster, R.C, and Cubley, J., 2020, The upper
157 mantle structure of northwestern Canada from teleseismic body wave tomography:
158 *Journal of Geophysical Research: Solid Earth*, v. 125, p. 1–18,
159 <https://doi.org/10.1029/2019JB018837>.

Francis, D., Minarik, W., Proenza, Y., and Shi, L., 2010, An overview of the Canadian Cordilleran lithospheric: Canadian Journal of Earth Sciences v. 47, p. 353-368.
<https://doi.org/10.1139/e09-072>.

Gibert, B., Seipold, U., Tommasi, A., and Mainprice, D., 2003, Thermal diffusivity of upper mantle rocks: Influence of temperature, pressure and the deformation fabric: Journal of Geophysical Research: Solid Earth, v. 108, B8, 2359,
<https://doi.org/10.1029/2002JB002108>.

Holland, T. J. B., and Powell, R., 2011, An improved and extended internally consistent thermodynamic dataset for phases of petrological interest, involving a new equation of state for solids: Journal of Metamorphic Geology, v. 29, p. 333-383,
<https://doi.org/10.1111/j.1525-1314.2010.00923.x>.

Liu, J., Brin, L.E., Pearson, G.D., Bretschneider, L., Luguët, A., van Acken, D., Kjarsgaard, B., Riches, A., and Mišković, A., 2018, Diamondiferous Paleoproterozoic mantle roots beneath Arctic Canada: A study of mantle xenoliths from Parry Peninsula and Central Victoria Island: Geochimica et Cosmochimica Acta, v. 239, p. 294-311,
<https://doi.org/10.1016/j.gca.2018.08.010>.

Ma, Z., Dalton, C.A., Russell, J.B., Gaherty, J.B., Hirth, G., and Forsyth, D.W., 2020, Shear attenuation and anelastic mechanisms in the central Pacific upper mantle: Earth and Planetary Science Letters, v. 536, p. 116-148, <https://doi.org/10.1016/j.epsl.2020.116148>.

Nelson, J., and Colpron, M, 2007, Tectonics and metallogeny of the British Columbia, Yukon and Alaskan Cordillera, 1.8 Ga to the present, *in* Goodfellow, W.D., eds., Mineral Deposits of Canada: A Synthesis of Major Deposit-Types, District Metallogeny, the

182 Evolution of Geological Provinces, and Exploration Methods: Geological Association of
183 Canada, Mineral Deposits Division, Special Publication No. 5, p. 755–791.

184 Rasendra, N., Bonnin, M., Mazzotti, S., and Tiberi, C., 2014, Crustal and upper-mantle
185 anisotropy related to fossilized transpression fabric along the Denali fault, northern
186 Canadian Cordillera: *Seismological Society of America Bulletin*, v. 104, p. 1964–1975,
187 <https://doi.org/10.1785/0120130233>.

188 Silver, P.G., and Chan, W.W., 1991, Shear wave splitting and subcontinental mantle
189 deformation: *Journal of Geophysical Research: Solid Earth*, v. 96, p. 16429–16454,
190 <https://doi.org/10.1029/91JB00899>.

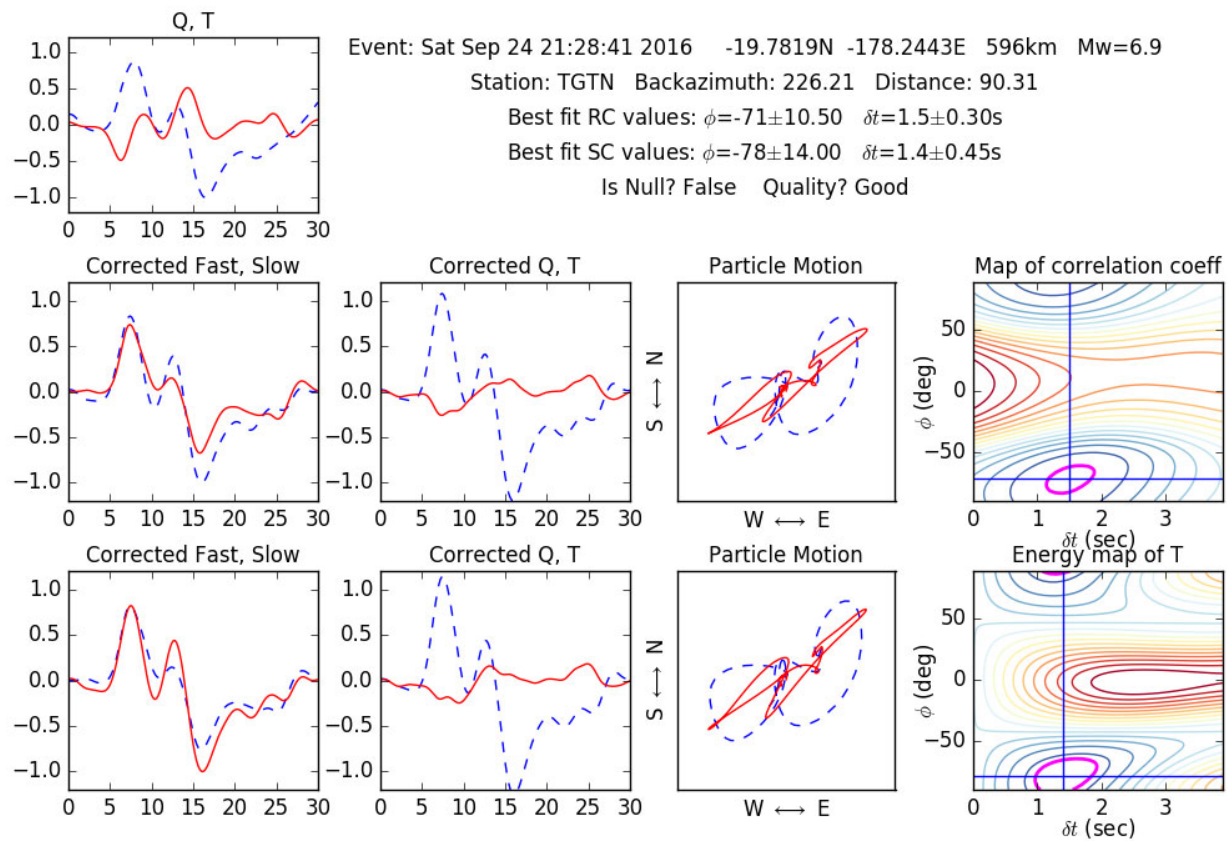
191 Snyder, D., and Bruneton, M., 2007, Seismic anisotropy of the Slave craton, NW Canada, from
192 joint interpretation of SKS and Rayleigh waves: *Geophysical Journal International*, v.
193 169, p. 170–188, <https://doi.org/10.1111/j.1365-246X.2006.03287.x>.

194 Stixrude, L., and Lithgow-Bertelloni, C., 2011, Thermodynamics of mantle minerals - II. Phase
195 equilibria: *Geophysical Journal International*, v. 184, p. 1180–1213,
196 <https://doi.org/10.1111/j.1365-246X.2010.04890.x>

197 VanDecar, J.C., 1991, Upper-mantle structure of the Cascadia subduction zone from nonlinear
198 teleseismic travel-time inversion (Unpublished doctoral dissertation). University of
199 Washington

200 Venereau, C.M.A., Martin-Short, R., Bastow, I.D., Allen, R.M., & Kounoudis, R., 2019, The
201 role of variable slab dip in driving mantle flow at the eastern edge of the Alaskan
202 subduction margin: Insights from shear-wave splitting: *Geochemistry, Geophysics,*
203 *Geosystems*, v. 20, 2433–2448. <https://doi.org/10.1029/2018GC008170>.

204 Wüstefeld, A., and Bokelmann, G., 2007, Null Detection in Shear-Wave Splitting
205 Measurements: Bulletin of the Seismological Society of America, v. 97, 4, p. 1204–1211.
206 <https://doi.org/10.1785/0120060190>.
207 Wüstefeld, A., Bokelmann, G., Zaroli, C., and Barruol, G., 2008, SplitLab: A shear-wave
208 splitting environment in Matlab: Computers & Geosciences, v. 34, p. 515–528.
209 <https://doi.org/10.1016/j.cageo.2007.08.002>.
210



211
 212 Figure DR1: Example of a single measurement at station TGTN. The top left panel shows the
 213 longitudinal (Q, blue) and tangential (T, red) seismograms where the time window is manually
 214 picked around the predicted SKS phase arrival. The text gives event details as well as splitting
 215 parameters resulting from the two techniques. The center and bottom panels display results for
 216 the RC and SC techniques, respectively. For each technique, from left to right, the first panel
 217 displays the fast (blue) and slow (red) components of the seismogram. The second and third
 218 panels display the radial (Q, blue) and tangential (T, red) components and the particle motion
 219 before (blue) and after (red) removing the effect of splitting, respectively. The fourth panel
 220 displays either the misfit map of correlation coefficient (RC technique) or the energy map of the
 221 tangential component (SC technique). Warm and cold colors represent high and low misfit
 222 values, respectively. The magenta contours show the 95% confidence interval.

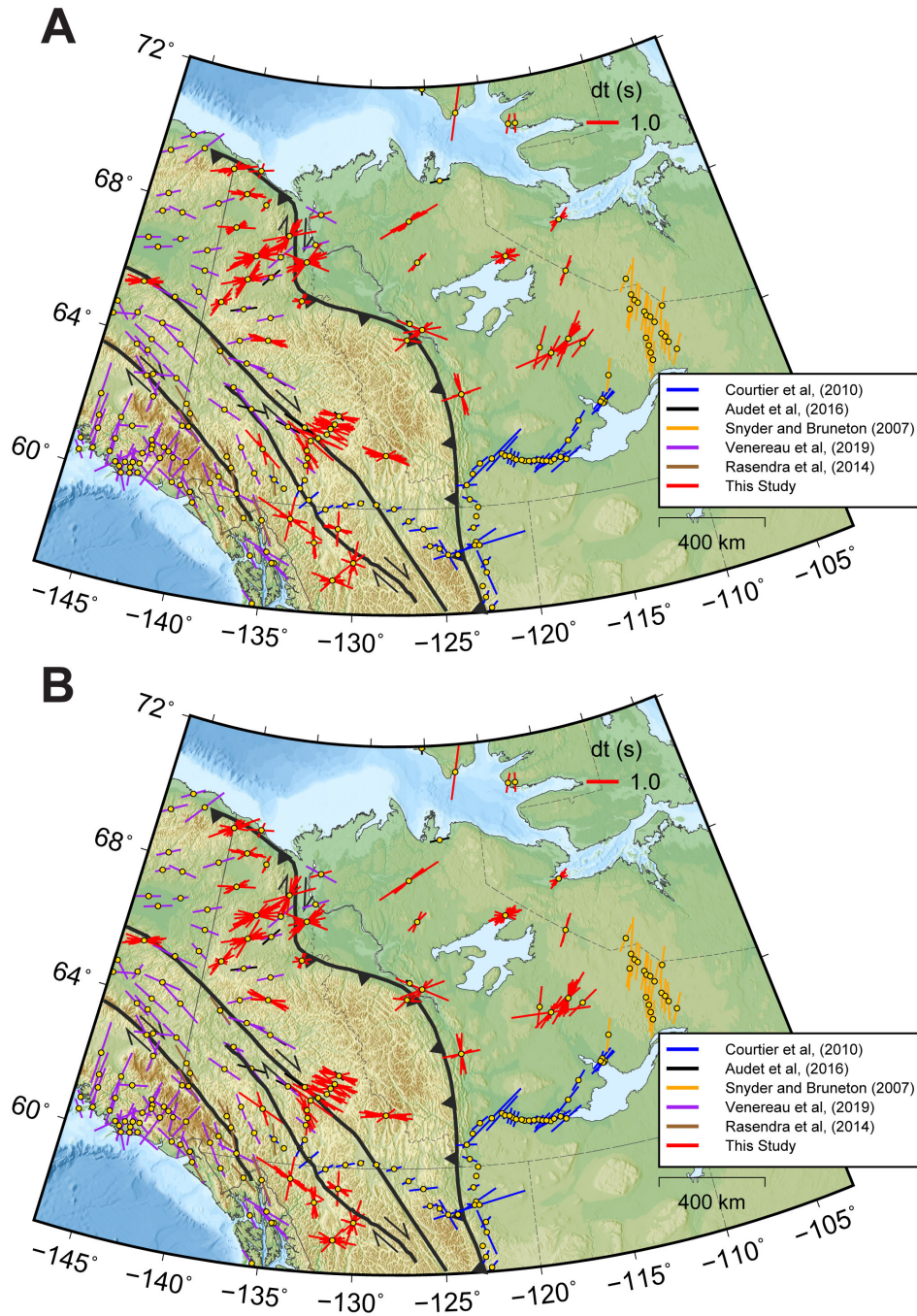
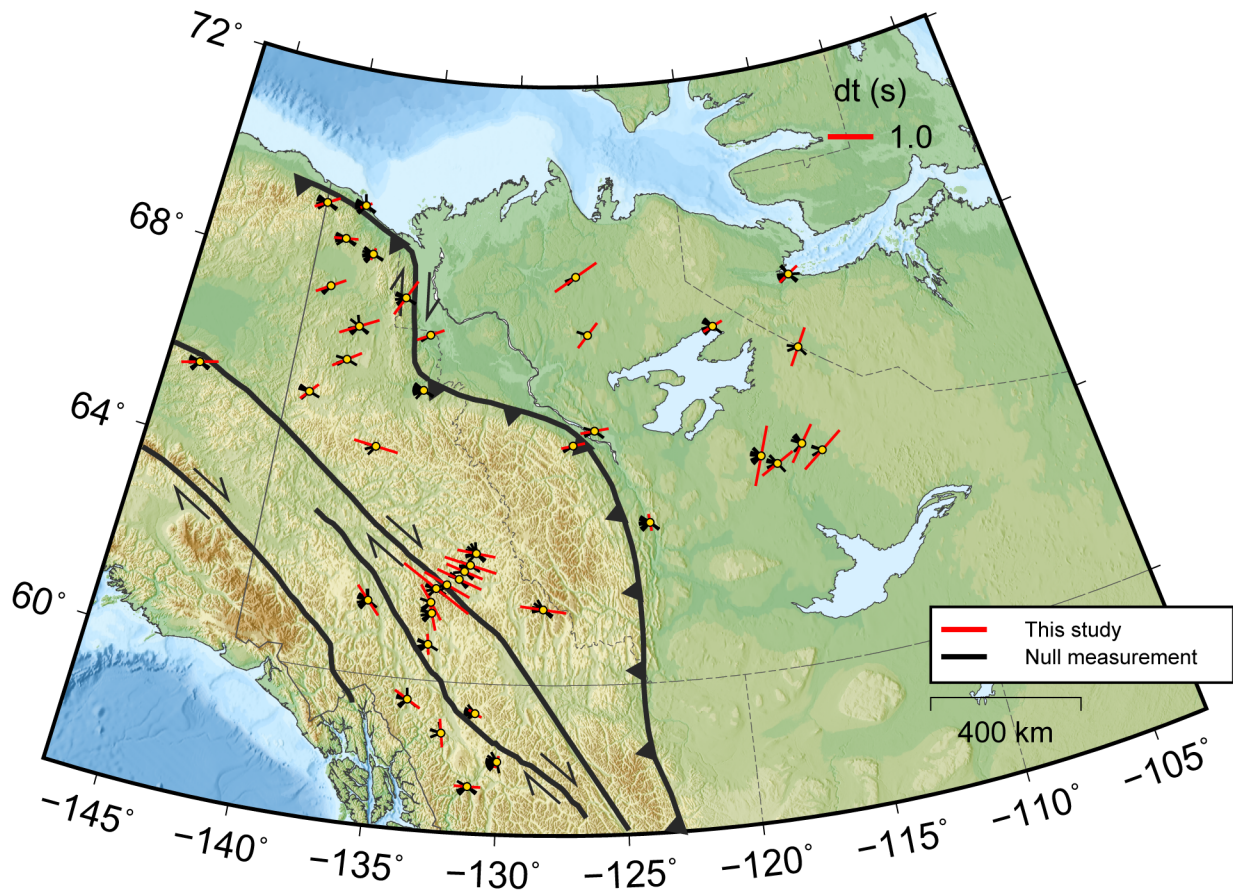


Figure DR2: Topographic map of northwestern Canada showing all “fair” and “good” non-null SKS splitting measurements (in red) for each station for the RC (A) and the SC (B) techniques. Also shown, the compiled estimates of shear wave splitting from Audet et al., (2016); Courtier et al., (2010); Rasendra et al., (2014); Snyder and Bruneton, (2007) and Venereau et al., (2019).



229

230 Figure DR3: Topographic map of northwestern Canada showing the average splitting parameters

231 (red) and all “fair” and “good” null measurements for each station (black).

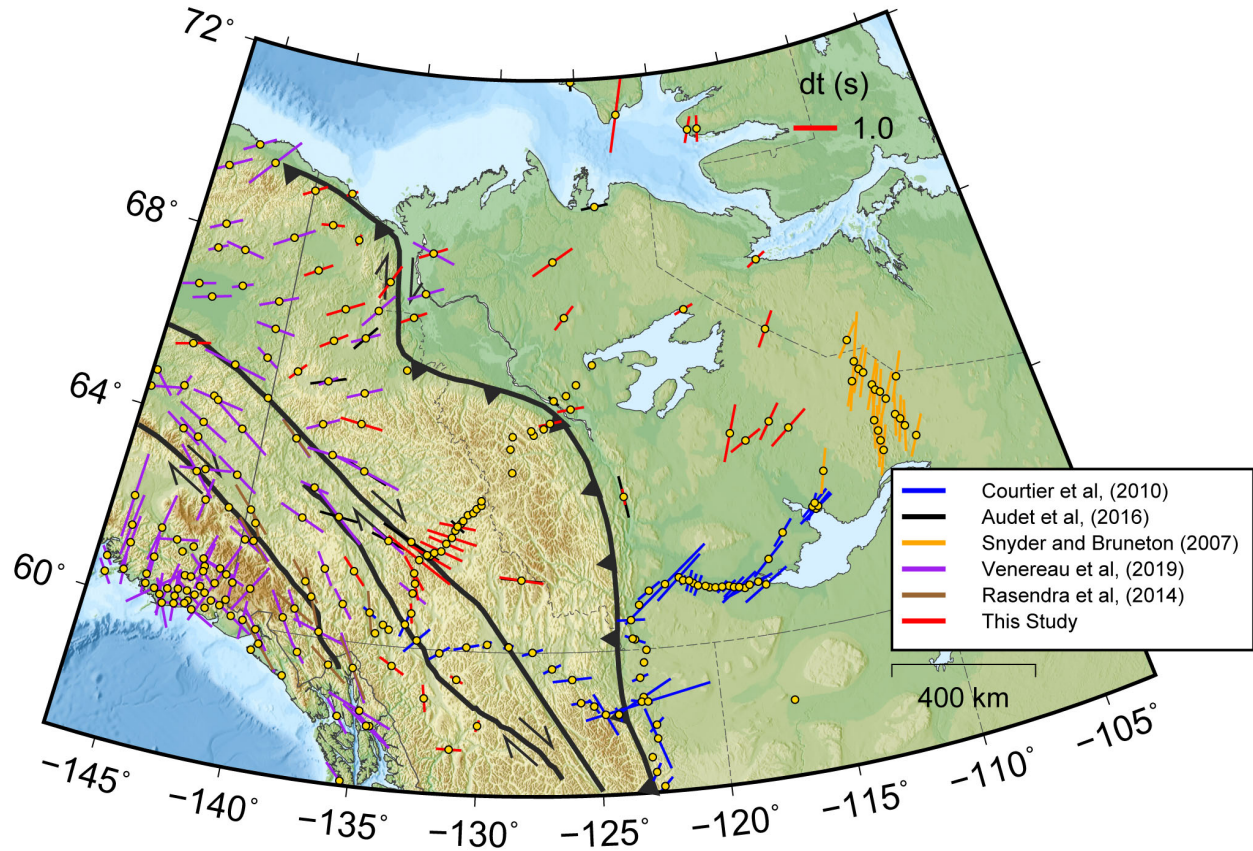
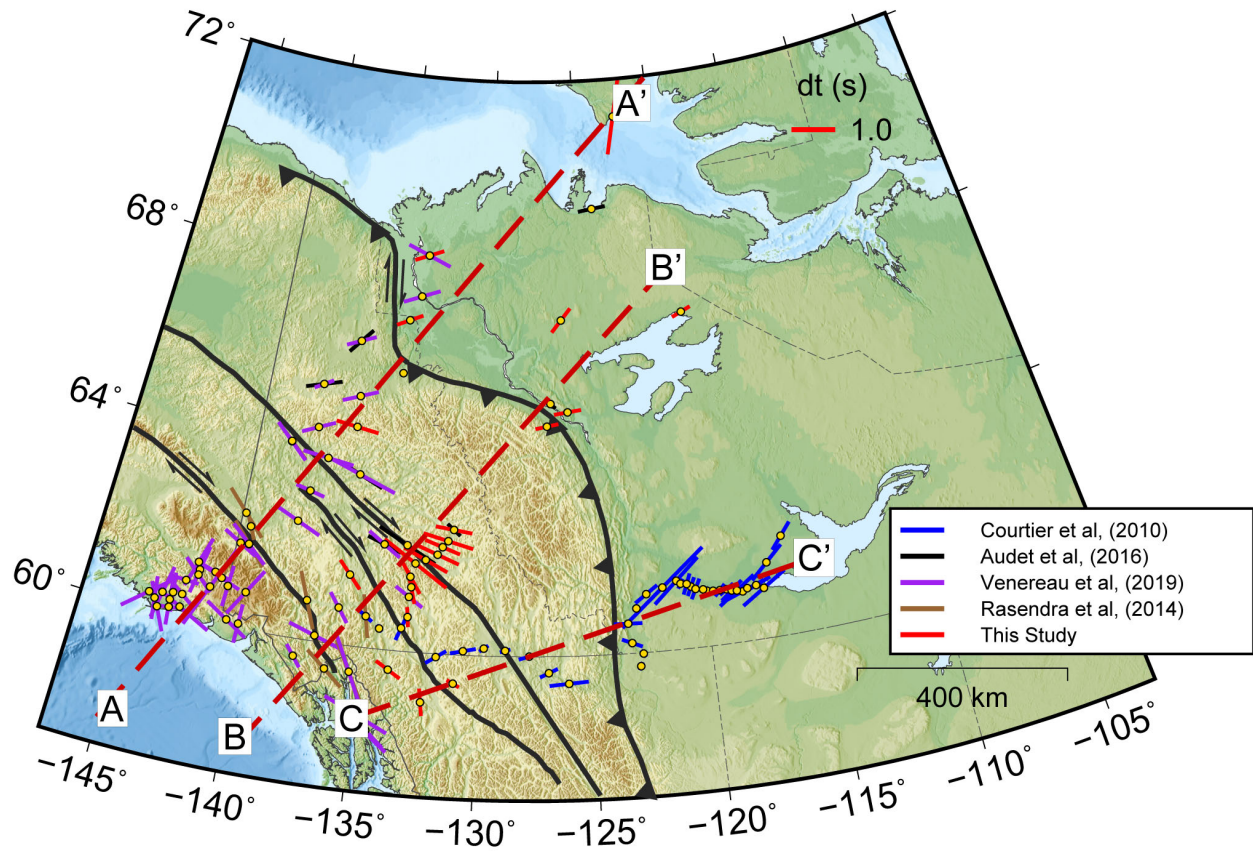


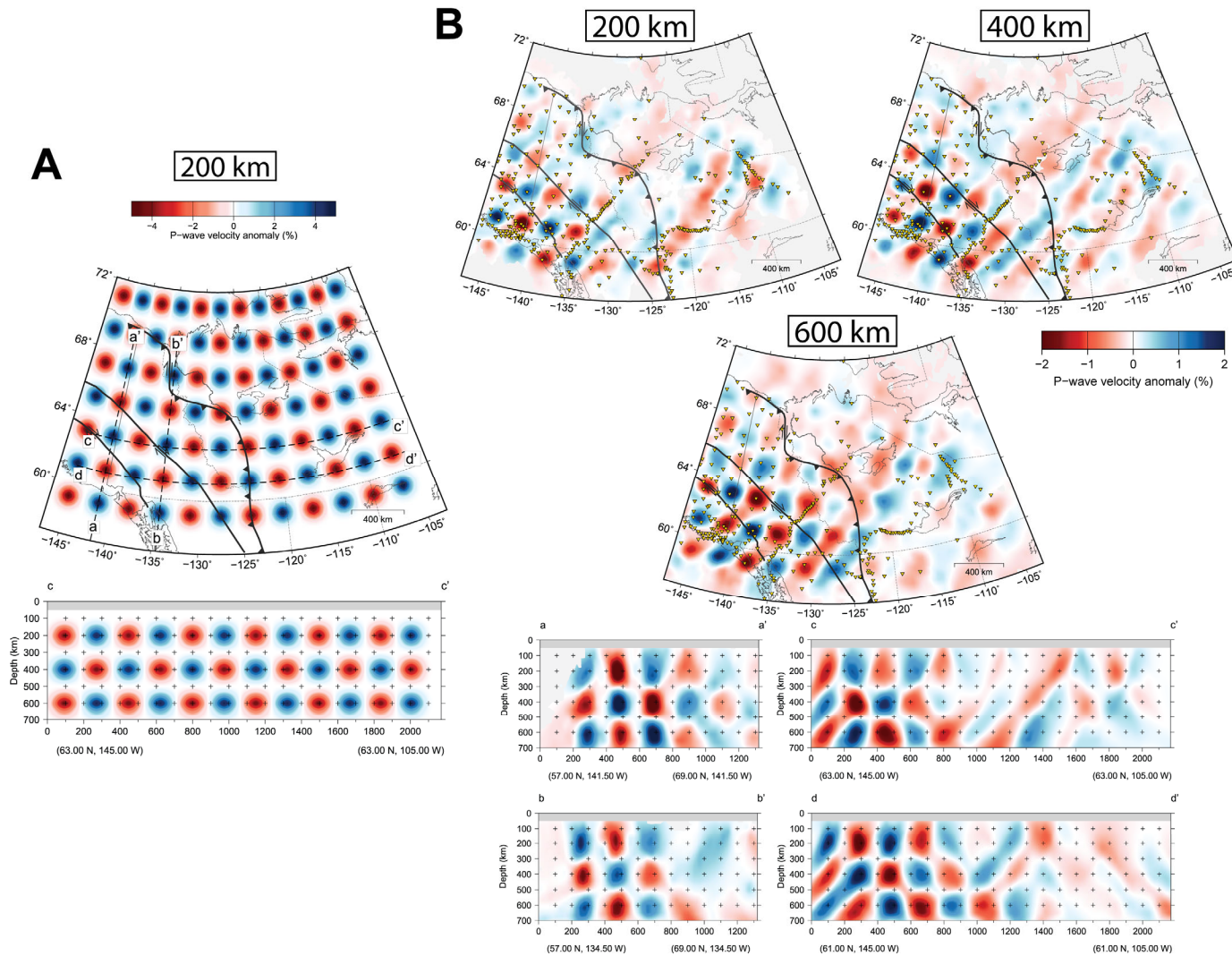
Figure DR4: Topographic map of northwestern Canada showing the average splitting parameters per station (red). Also shown, the compiled estimates of shear wave splitting from Audet et al., (2016); Courtier et al., (2010); Rasendra et al., (2014); Snyder and Bruneton, (2007) and Venereau et al., (2019).



238

239 Figure DR5: Topographic map of northwestern Canada showing the stations for which the

240 splitting parameters are projected along cross sections A-A', B-B' and C-C' (Figure 3).



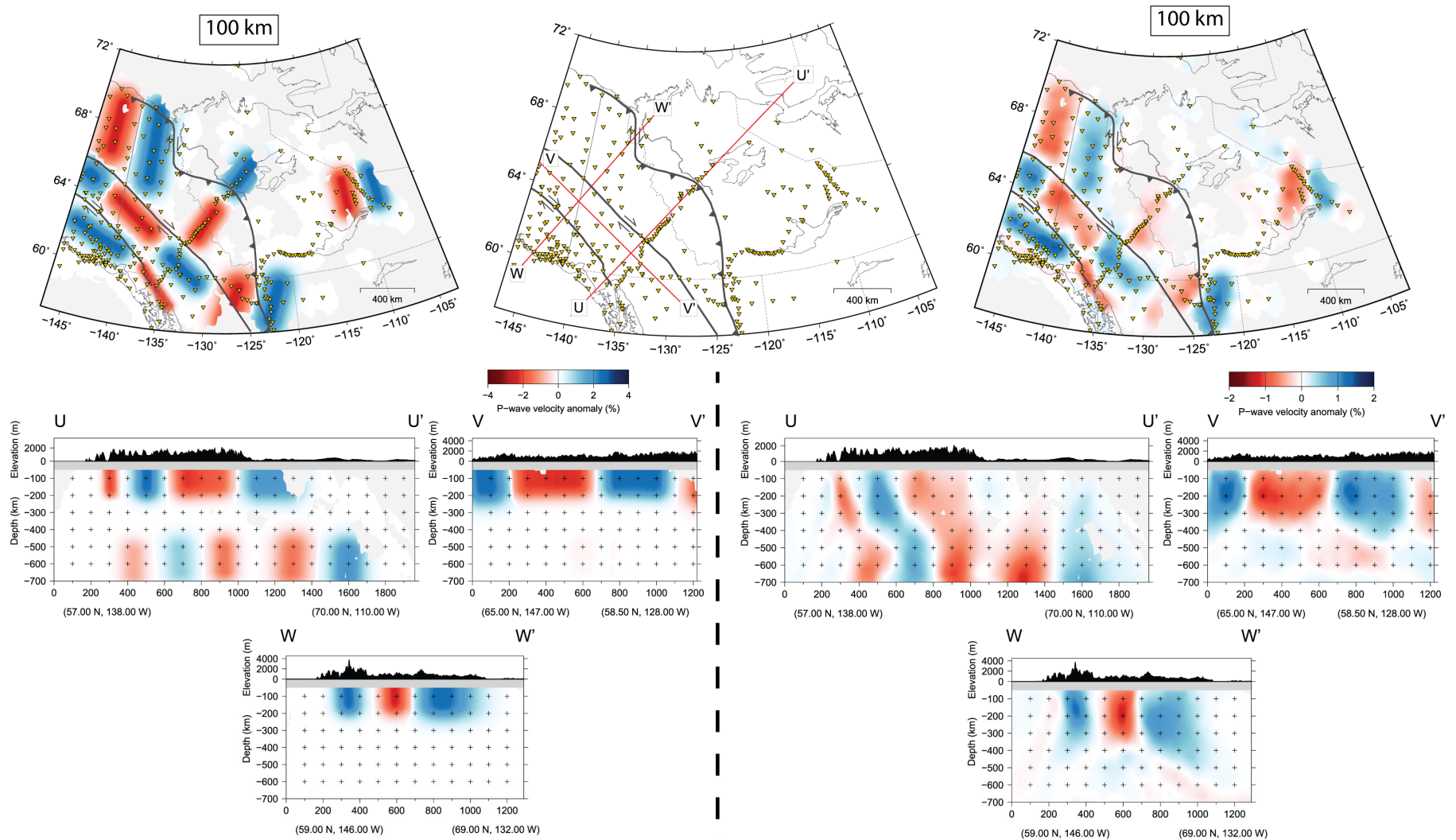
241

242 Figure DR6: P-wave checkerboard test. **A:** Input map and cross section c-c' showing the distribution of synthetic anomalies through the

243 input checkerboard model. Cross section locations are displayed on the 200 km depth slice. **B:** Output maps and cross sections through the

244 retrieved checkerboard model at 200, 400 and 600 km depth. Areas with less than 4 ray hits are displayed in light gray and the first 50 km

245 are masked. Note the excellent recovery in the western region of the P-wave model.



246

247 Figure DR7: P-wave structural test. Cross sections and depth slices through the P-wave structural resolution test. Structural resolution test
 248 showing input anomalies (left) and output anomalies (right) through the output structural P-wave model. Synthetic anomalies are defined by
 249 Gaussian functions across their widths. Areas with less than 4 ray hits are displayed in light gray and the first 50 km are masked. Note the
 250 excellent lateral resolution in the western region of the P-wave model.

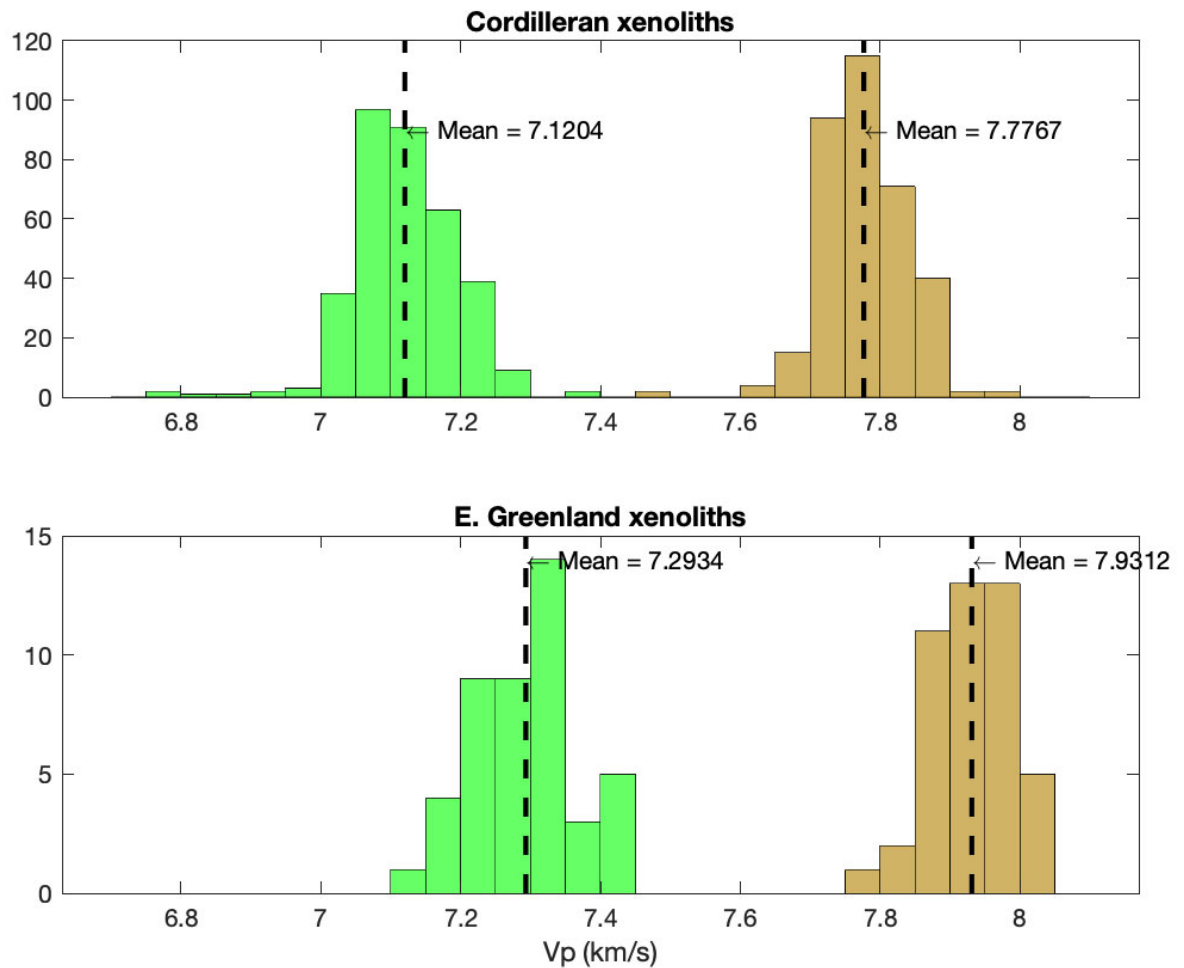


Figure DR8: Histograms of estimated P-wave velocities for two different xenolith populations, using two different thermodynamic databases. Top subplot shows velocities for Cordilleran xenoliths (Francis et al., 2010), and bottom shows east Greenland samples, representative of cratonic compositions (Canil, 2004). The shift between the same color histograms between the top and the bottom plots provides an estimate of the magnitude of potential compositionally caused velocity changes.

Table DR1: Station average splitting parameters

Stations					Average Station Parameter			
Network	Name	#	Lat (°)	Lon (°)	Φ (°)	σ_{Φ}	Δt (s)	$\sigma_{\delta t}$
TA	D27M	17	69.243	-140.965	61.6412	6.945	0.6018	0.1448
TA	D28M	2	69.3286	-138.737	61.9368	19.8632	0.2761	0.3471
TA	E28M	11	68.6043	-139.535	84.3616	8.6143	0.5361	0.1583
TA	E29M	3	68.3889	-137.897	14.7276	27.9602	0.2765	0.5898
TA	F28M	6	67.6136	-139.872	60.5468	11.2174	0.7055	0.2602
TA	F30M	9	67.6106	-135.786	29.7252	6.5961	0.8989	0.1496
TA	G29M	27	66.9116	-138.022	64.6524	5.2003	0.9239	0.1271
TA	G31M	22	66.9227	-134.271	65.4438	6.5537	0.6352	0.1033
TA	H29M	15	66.2191	-138.369	58.9283	11.8714	0.7058	0.2467
TA	H31M	8	65.8052	-134.343	41.665	10.039	0.1652	0.1707
TA	I28M	7	65.4483	-139.936	43.3278	9.6396	0.5062	0.1439
TA	J30M	13	64.5753	-136.33	-80.7745	7.7921	0.9998	0.1841
TA	N31M	4	61.4862	-135.78	-40.5946	14.0452	0.8047	0.31
TA	P32M	7	59.5898	-133.715	-58.4571	9.8456	0.6767	0.2571
TA	Q32M	9	58.9601	-132.269	-8.062	8.8326	0.6284	0.1734
TA	R33M	8	59.3946	-130.967	-61.8987	14.3514	0.3275	0.2698
TA	S34M	10	57.9128	-131.131	-88.8816	8.9724	0.5867	0.2262
NY	MMPY	7	62.6189	-131.263	-81.9853	9.7238	0.8565	0.2184
NY	NLHD	1	71.2509	-122.333	12.299	37.9	1.750	0.500
NY	PYRD	3	64.8212	-126.907	78.5366	14.8631	0.538	0.4427
NY	TGTN	21	61.5267	-128.273	-82.2022	5.1074	1.021	0.1111

Stations					Average Station Parameter			
Network	Name	#	Lat (°)	Lon (°)	Φ (°)	σ_{Φ}	Δt (s)	$\sigma_{\delta t}$
NY	TULN	4	65.1147	-125.855	81.4116	14.7038	0.63	0.4488
NY	ULUN	1	70.7532	-117.185	7.207	54.462	0.605	1.163
NY	WGLY	8	63.2281	-123.458	-6.8802	8.7427	0.3745	0.2629
PO	CLVN	2	67.039	-126.078	39.0334	16.0122	0.6915	0.2858
PO	CTLN	26	64.4287	-116.019	36.0453	4.6633	0.9406	0.1112
PO	DHRN	20	67.0331	-119.509	66.2771	6.2512	0.4697	0.1254
PO	GALN	5	64.1167	-117.314	60.6964	10.3699	0.8566	0.2024
PO	HPLN	2	66.3485	-115.323	30.3082	14.2489	0.8963	0.2816
PO	ILKN	1	64.2241	-115.129	53	15.5	1.15	0.45
PO	ROMN	1	64.3157	-118.018	19.5	28	1.35	0.75
PO	SMPN	8	68.2107	-126.654	56.2018	7.5246	1.1124	0.1823
CN	DLBC	7	58.4372	-130.027	15.8806	9.8692	0.2746	0.249
CN	HMNT	1	70.7631	-117.806	18.655	10.400	0.62	0.19
CN	INK	1	68.307	-133.53	68.31	38.97	0.69	0.32
CN	KUKN	8	67.8226	-115.09	57.5024	8.3744	0.5257	0.1497
7C	MM07	2	60.7272	-133.071	-7.0275	22.2913	0.4617	0.469
7C	MM09	4	61.3568	-133.021	-15.8346	9.5509	0.7748	0.1882
7C	MM10	3	61.5744	-133.091	-33.5526	13.7643	0.8928	0.3213
7C	MM11	1	61.8624	-132.915	-56.5	15.75	1.8	0.675
7C	MM12	6	61.9525	-132.461	-64.561	9.2019	1.1393	0.22
7C	MM17	5	62.0789	-131.948	-68.9756	7.6344	1.0641	0.1999

Stations					Average Station Parameter			
Network	Name	#	Lat (°)	Lon (°)	Φ (°)	σ_{Φ}	Δt (s)	$\sigma_{\delta t}$
7C	MM18	5	62.2424	-131.734	-70.8528	9.0801	0.8617	0.2106
7C	MM19	9	62.3754	-131.495	-75.7245	7.3741	1.1952	0.1825
AK	PPD	14	65.5174	-145.525	74.0115	7.5492	0.8189	0.1759